molecules

MDPI

Article

Preparation of MoFs-Derived Cobalt Oxide/Carbon Nanotubes Composites for High-Performance Asymmetric Supercapacitor

Caiqin Yang [1,2], Weiwei Li [3], Xiaowei Liu [3], Xiumei Song [1,*], Hongpeng Li [4] and Lichao Tan [1,2,3,5,*]

[1] Institute of Carbon Neutrality, Zhejiang Wanli University, Ningbo 315100, China
[2] School of Materials Science and Chemical Engineering, Harbin University of Science and Technology, Harbin 150040, China
[3] Chilwee Power Co., Ltd., No. 18 Chengnan Road, Huaxi Industrial Zone, Changxing 313100, China
[4] College of Mechanical Engineering, Yangzhou University, Yangzhou 225127, China
[5] State Key Laboratory of Clean Energy Utilization, School of Materials Science and Engineering, Zhejiang University, Hangzhou 310027, China
* Correspondence: songxm_hit@163.com (X.S.); lctan@hrbust.edu.cn (L.T.)

Abstract: Metal–organic frameworks (MOFs)-derived metallic oxide compounds exhibit a tunable structure and intriguing activity and have received intensive investigation in recent years. Herein, this work reports metal–organic frameworks (MOFs)-derived cobalt oxide/carbon nanotubes (MWCNTx@Co_3O_4) composites by calcining the MWCNTx@ZIF-67 precursor in one step. The morphology and structure of the composite were investigated by scanning electron microscope (SEM) and transmission electron microscope (TEM) characterization. The compositions and valence states of the compounds were characterized by X-ray diffraction (XRD) and X-ray photoelectron spectroscopy (XPS). Benefiting from the structurally stable MOFs-derived porous cobalt oxide frameworks and the homogeneous conductive carbon nanotubes, the synthesized MWCNTx@Co_3O_4 composites display a maximum specific capacitance of 206.89 $F{\cdot}g^{-1}$ at 1.0 $A{\cdot}g^{-1}$. In addition, the specific capacitance of the $MWCNT_3$@Co_3O_4//activated carbon (AC) asymmetric capacitor reaches 50 $F{\cdot}g^{-1}$, and has an excellent electrochemical performance. These results suggest that the MWCNTx@Co_3O_4 composites can be a potential candidate for electrochemical energy storage devices.

Keywords: asymmetric supercapacitor; electrode materials; MOFs derivatives; cobalt compounds; carbon nanotubes

Citation: Yang, C.; Li, W.; Liu, X.; Song, X.; Li, H.; Tan, L. Preparation of MoFs-Derived Cobalt Oxide/Carbon Nanotubes Composites for High-Performance Asymmetric Supercapacitor. *Molecules* **2023**, *28*, 3177. https://doi.org/10.3390/molecules28073177

Academic Editor: Lihua Gan

Received: 28 February 2023
Revised: 28 March 2023
Accepted: 30 March 2023
Published: 3 April 2023

1. Introduction

The desire to reduce society's dependence on fossil fuels has made the exploration of new energy and high energy utilization efficiency one of the most important issues faced by national governments in the 21st century. Energy storage, which is an intermediate step toward the efficient utilization of energy, has attracted large-scale concern and increasing research interest [1]. Among various emerging energy storage technologies, supercapacitors (SCs), also known as electrochemical capacitors (ECs), are a new concept of energy storage devices that was developed at the forefront of the available environmentally friendly electrochemical energy storage systems. According to the energy storage mechanisms, there are two types of supercapacitors: electrical double-layer capacitors (EDLCs) and pseudocapacitors. The core of supercapacitors is the electrode material, which directly dominates the performance of energy storage [2–18].

In recent years, pseudocapacitors based on transition metal oxides/hydroxides with variable valence exhibit a higher specific capacitance. Moreover, transition metal oxides and hydroxides have attracted extensive interest due to their high theoretical capacity, low cost, environmental friendliness and great flexibility in morphology and structures, such as Co_3O_4, NiO, Fe_3O_4 and MnO_2 for pseudocapacitor electrodes, which achieve ultrahigh values of electrode capacitance [19–26]. Among the transition metal oxides, due to its

wide potential range, low cost and environmental friendliness, Co_3O_4 has attracted much attention for its good catalysis, adsorptive behavior and electrochromic applications [27–29]. However, Co_3O_4 systems are limited by several adverse factors, such as a poor electrical conductivity and volume changes during the cycle process, a poor reversibility and a degradation in capacity at higher current densities [30]. Therefore, the rational design of sophisticated electrode structures that accelerate the charge transfer and enable the sufficient exposure of the surface active site is highly essential for Co_3O_4-based materials to achieve high-performance supercapacitors.

In addition, the main electrode materials, carbon materials, have been deeply studied with the widening of the application areas of supercapacitors because of their high surface area, chemical stability, electrical conductivity and low cost [31–36]. Carbon nanotubes, graphene, template carbon and carbide-derived carbon have been widely used in EDLCs.

In our study, we demonstrate a simple and economic strategy for the preparation of an MWCNTx@Co_3O_4 composite. This composite has a large surface area, which enables the effective exposure of the active site for the Faradaic redox reaction and obviously promotes the charge transfer process, and the diamond dodecahedron structure of the MWCNTx@Co_3O_4 composite can promote the deep ion diffusion among electrode materials. As a result, the MWCNTx@Co_3O_4 composite exhibits a high specific capacitance of 206.89 $F{\cdot}g^{-1}$ at a current density of 1.0 $A{\cdot}g^{-1}$. Moreover, the specific capacitance of the $MWCNT_3$@Co_3O_4//AC asymmetric capacitor reaches 50 $F{\cdot}g^{-1}$, and has an excellent electrochemical performance. Therefore, the MWCNTx@Co_3O_4 composite can be considered as promising materials for high-performance electrochemical capacitors.

2. Results and Discussion

The SEM of the MWCNTx@Co_3O_4 sample is shown in Figure 1. As can be seen from Figure 1a–d, Co_3O_4 in MWCNTx@Co_3O_4 samples all show a rhomboidal dodecahedron morphology, indicating that Co_3O_4 retains the morphology of ZIF-67 and is not damaged by high temperature. The dispersion of MWCNT in $MWCNT_1$@Co_3O_4 and $MWCNT_2$@Co_3O_4 samples was also observed because the content of carbon nanotubes was less than that of Co_3O_4. On the other hand, it is possible that the surface oxidation of MWCNT has oxygen-containing functional groups that repel each other under electrostatic action so that the agglomeration of MWCNT is greatly reduced [37]. As can be seen from Figure 1d, because the MWCNT content is the highest, the whole $MWCNT_4$@Co_3O_4 sample is wrapped by MWCNT, resulting in the Co_3O_4 polyhedron structure not being obvious. It even hindered the growth of the polyhedral structure, and the morphology distribution was uneven, which may be determined by the growth mechanism of ZIF-67 on the MWCNT surface. However, the distribution of MWCNTS in $MWCNT_3$@Co_3O_4 is more reasonable, as shown in Figure 1c. The length and diameter of MWCNTs is 500 nm and 20 nm, respectively. The Co_3O_4 rhomboidal dodecahedron is clear and uniform in size, and the MWCNT is evenly dispersed. This phenomenon may be caused by the growth mechanism of MWCNTx@ZIF-67: under the action of a PVP dispersant, MWCNT is uniformly dispersed and can only adsorb a certain amount of Co^{2+} on the surface, while the content of ZIF-67 crystal is fixed and, after calcination, uniformly dispersed $MWCNT_3$@Co_3O_4 [38] is obtained. According to the above characterization analysis, the morphology of the $MWCNT_3$@Co_3O_4 composite is the most uniform.

The microstructure and composite structure of $MWCNT_3$@Co_3O_4 were further studied by TEM characterization, as shown in Figure 2. Figure 2a,b show low and high-magnification TEM images of $MWCNT_3$@Co_3O_4. It can be seen that the Co_3O_4 surface is connected to MWCNT. This composite structure can improve the conductivity of Co_3O_4, thereby enhancing its electrochemical performance. The size of cobalt oxide in $MWCNT_3$@Co_3O_4 is between 120–350 nm, consistent with the size captured in the SEM image. Figure 2c is the high-resolution transmission electron microscope image of the $MWCNT_3$@Co_3O_4 sample. Lattice fringes of different widths were obtained by analyzing the lattice spacing, and were 0.239 nm (the (311) crystal plane of Co_3O_4 nanoparticles)

and 0.29 nm (the (220) crystal plane of Co_3O_4 nanoparticles), respectively. The polycrystalline properties of $MWCNT_3@Co_3O_4$ composites are described. Figure 2d is the selected electron diffraction diagram of the $MWCNT_3@Co_3O_4$ composite material, which indicates four bright concentric diffraction rings. The radius of the diffraction ring corresponds to the crystal surfaces of the cubic Co_3O_4 nanoparticles (511), (400), (200) and (311), which are consistent with the XRD results, and also indicate the polycrystalline property of the material. In summary, the successful preparation of $MWCNT_3@Co_3O_4$ composite materials is indicated by the above experimental results.

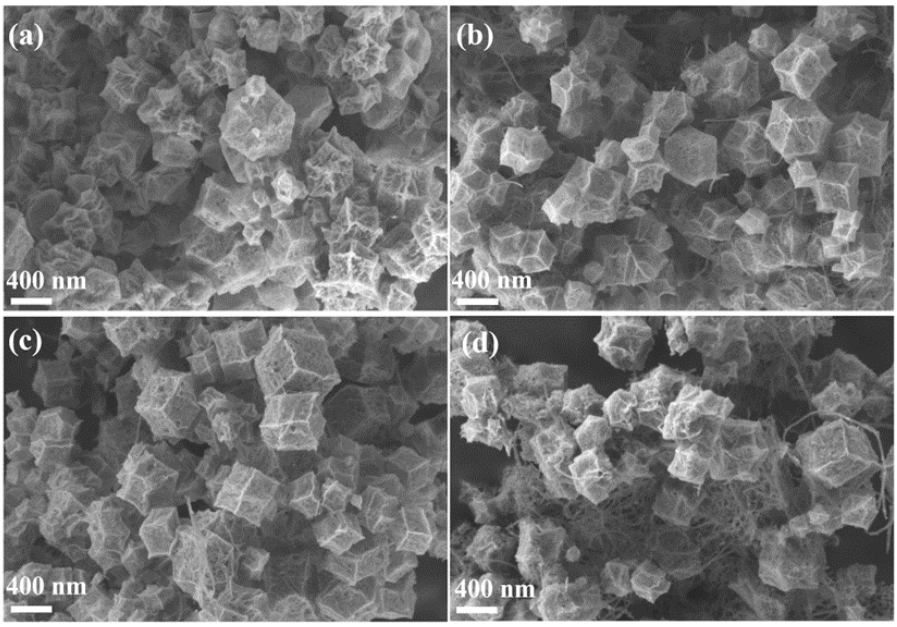

Figure 1. Different MWCNT additions, $MWCNTx@Co_3O_4$. SEM diagram of nanocomposites: (**a**) $MWCNT_1@Co_3O_4$; (**b**) $MWCNT_2@Co_3O_4$; (**c**) $MWCNT_3@Co_3O_4$; (**d**) $MWCNT_4@Co_3O_4$.

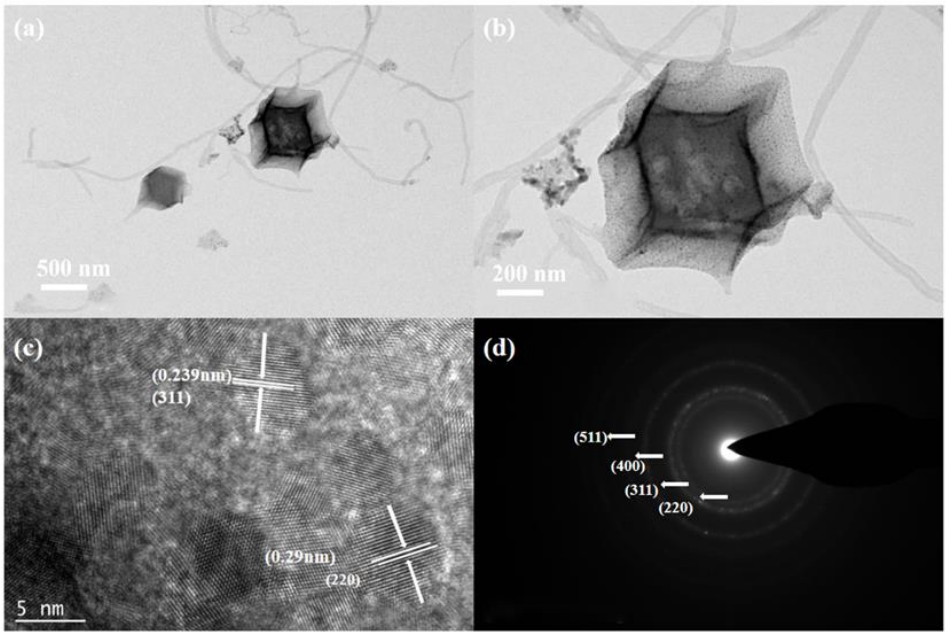

Figure 2. (**a**,**b**) TEM diagrams at different magnifications of $MWCNT_3@Co_3O_4$; (**c**,**d**) high-resolution transmission electron microscopy (HRTEM) and selected area electron diffraction (SAED) of $MWCNT_3@Co_3O_4$.

The EDS analysis method was used to obtain the element composition and distribution map of the $MWCNT_3@Co_3O_4$ composite. It can be observed from Figure 3 that the content of the C element is the highest, which is mainly attributed to the conversion of the organic skeleton into a C source after calcination in ZIF and the addition of an appropriate amount of MWCNT. It can also be observed that Co and O elements are evenly distributed on the surface of the polyhedron structure, which confirms the existence of Co_3O_4, which is the basic condition for obtaining a good pseudocapacitance performance.

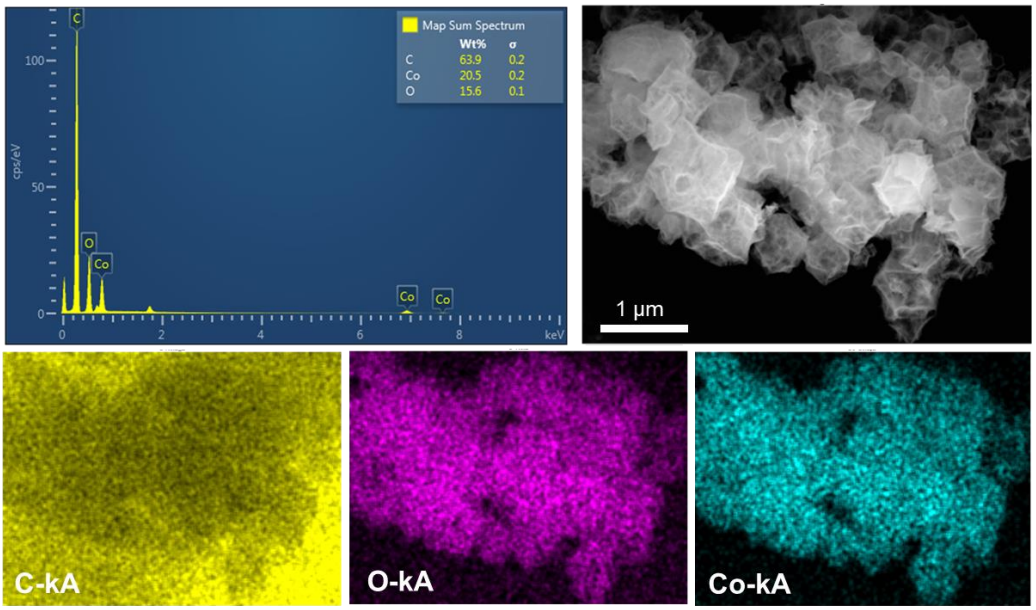

Figure 3. EDS analysis graph of $MWCNT_3@Co_3O_4$.

Table 1 shows the composite ratio of $MWCNT@Co_3O_4$. As can be seen from the table, with an increase in the amount of MWCNT added, the content of the C element in the composites gradually increased from 21.23% to 28.50%, whereas the content of the Co element in the composites gradually decreased from 50.65% to 44.32%. This confirms the addition of MWCNT. Through the above analysis, the successful synthesis of the $MWCNT_x@Co_3O_4$ composite materials is confirmed.

Table 1. Element content analysis of different compound ratios of $MWCNT@Co_3O_4$.

Sample	Element Type and Content Wt%			Total Elements
	C	Co	O	
$MWCNT_1@Co_3O_4$	21.23	50.65	28.12	100%
$MWCNT_2@Co_3O_4$	26.07	44.04	29.90	100%
$MWCNT_3@Co_3O_4$	27.50	45.20	27.30	100%
$MWCNT_4@Co_3O_4$	28.50	44.32	27.18	100%

Figure 4a,b are XRD patterns of the preparation precursor MWCNTx@ZIF-67 and the $MWCNTx@Co_3O_4$ sample after calcination in air. As can be seen from Figure 4a, MWCNTx@ZIF-67 has obvious 7.2° (011), 10.4° (002), 12.7° (112), 14.7° (022), 16.4° (013), 18.1° (222), 22.1° (114), 24.5° (233), 26.5° (134), 29.6° (044), 31.3° (244), and characteristic peaks of 32.5° (235) and 43.1° (100) that are consistent with those reported in the literature [39], which proves the successful synthesis of the MWCNTx@ZIF-67 precursor. The XRD results of $MWCNTx@Co_3O_4$ are shown in Figure 4b. As can be seen from the picture, $MWCNT_1@Co_3O_4$, $MWCNT_2@Co_3O_4$, $MWCNT_3@Co_3O_4$ and $MWCNT_4@Co_3O_4$ have (511), (400), (200), (111), (311) and (422) crystal plane diffraction peaks consistent with Co_3O_4 (JCPDS card number 74-2120). It is proved that the $MWCNTx@Co_3O_4$ sample was

successfully obtained after calcination. In addition, it can be seen from the XRD pattern of the MWCNTx@Co_3O_4 composite that the carbon-derived peak (002) is not obvious, which may be caused by the relatively large the diffraction peak intensity of Co_3O_4 on the one hand and the low crystallinity of carbon after calcining MWCNTx@ZIF-67 on the other hand.

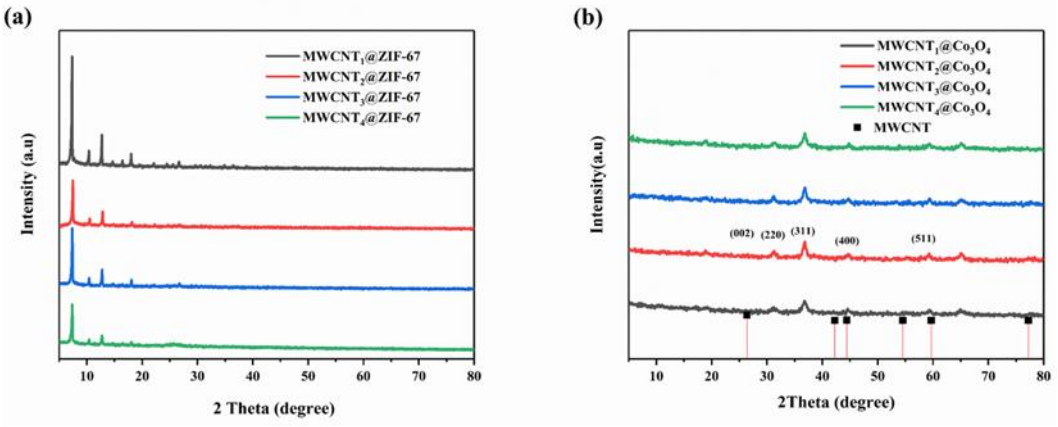

Figure 4. (**a**) XRD spectrum of MWCNTx@ZIF-67; (**b**) XRD spectrum of MWCNTx@Co_3O_4.

The chemical composition and corresponding valence states of the MWCNT$_3$@Co_3O_4 composite were studied by means of XPS characterization. All XPS maps were standardized with reference to the C 1s peak (284.6 eV). Figure 5a shows the full XPS spectrum of the MWCNT$_3$@Co_3O_4 composite, which mainly contains C, O and Co elements. As can be seen from the Co 2p map in Figure 5b, 779.9 eV and 796.6 eV correspond to Co 2p3/2 and Co 2p1/2, respectively, which are two peaks of Co^{2+} and Co^{3+}, and the experimental results are consistent with the literature [40]. As can be seen from the C 1s map in Figure 5c, there are three obvious characteristic peaks at 284.3, 285.8 and 286.4 eV. The peaks at 284.3 eV and 285.8 eV belong to C-C and C=C, respectively, whereas the peaks at 284.6 eV may belong to Co-O-C [41]. Figure 5d shows the O1s map, which mainly contains three peaks of 533.5 eV, 531.5 eV and 530.0 eV, among which the peaks of 530.0 eV and 531.5 eV belong to lattice oxygen species and surface-adsorbed oxygen [42]. These results further confirm the successful synthesis of composite materials, and are further consistent with XRD and EDS results.

Figure 6 shows the pore structure and specific surface area of the MWCNT$_x$@Co_3O_4 composites. As can be seen from Figure 6a, the adsorption/desorption isotherm of MWCNT$_x$@Co_3O_4 slowly rises at first, and, when it reaches a certain pressure, it rises sharply, resulting in a vertical tail ring and a hysteresis ring. This feature indicates that MWCNT$_x$@Co_3O_4 composite materials have microporous, mesoporous and macroporous structures. The specific surface areas of MWCNT$_1$@Co_3O_4, MWCNT$_2$@Co_3O_4, MWCNT$_3$@Co_3O_4 and MWCNT$_4$@Co_3O_4 are 104.20, 66.44, 99.56 and 136.97 $m^2 \cdot g^{-1}$, respectively. In addition, the pore diameter distribution curve of MWCNT$_x$@Co_3O_4 is shown in Figure 6b. The pore volumes of MWCNT$_1$@Co_3O_4, MWCNT$_2$@Co_3O_4, MWCNT$_3$@Co_3O_4 and MWCNT$_4$@Co_3O_4 were 3.39, 3.79, 3.06 and 3.30 nm, respectively. It can be well seen in the figure that the pore size distribution of MWCNT$_3$@Co_3O_4 is mainly mesoporous, mainly due to the insertion of MWCNTs into Co_3O_4, resulting in a larger pore size of the overall material. Furthermore, the mesoporous structure is conducive to ion diffusion, thereby improving the electrochemical performance of the material. Therefore, the obtained electrode material should have a good electrochemical performance.

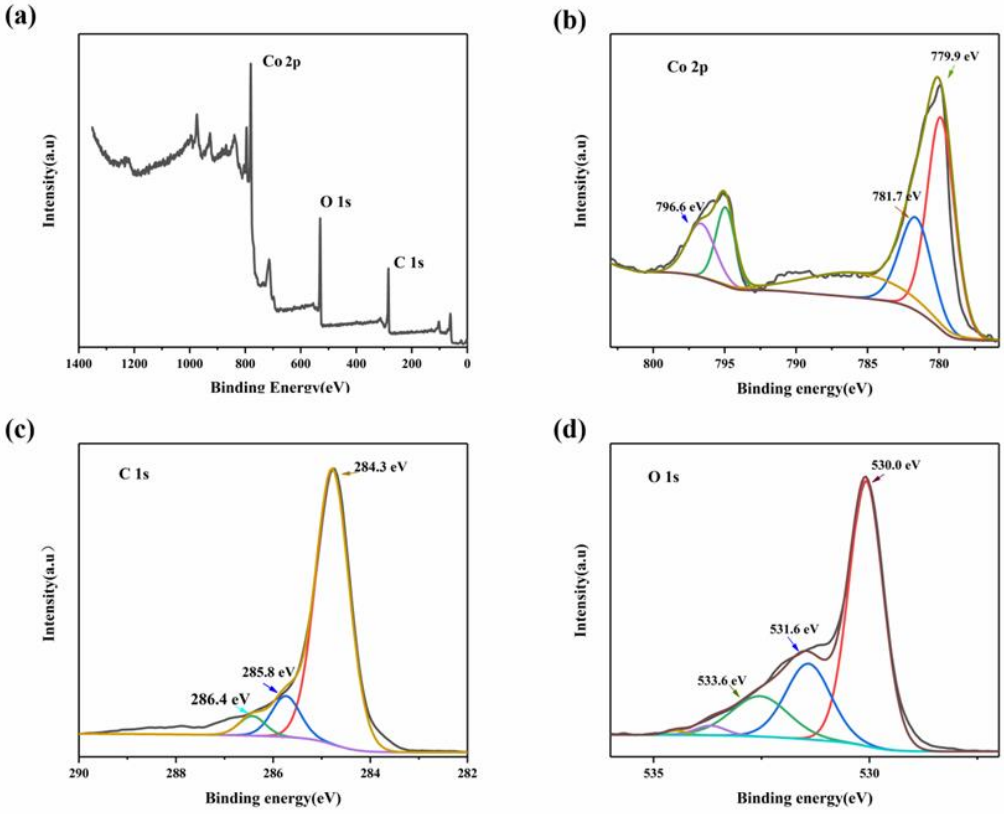

Figure 5. MWCNT3@Co_3O_4 (**a**) XPS full spectrum; (**b**) Co 2p; (**c**) C 1s and (**d**) O 1s XPS spectrum of fine spectrum.

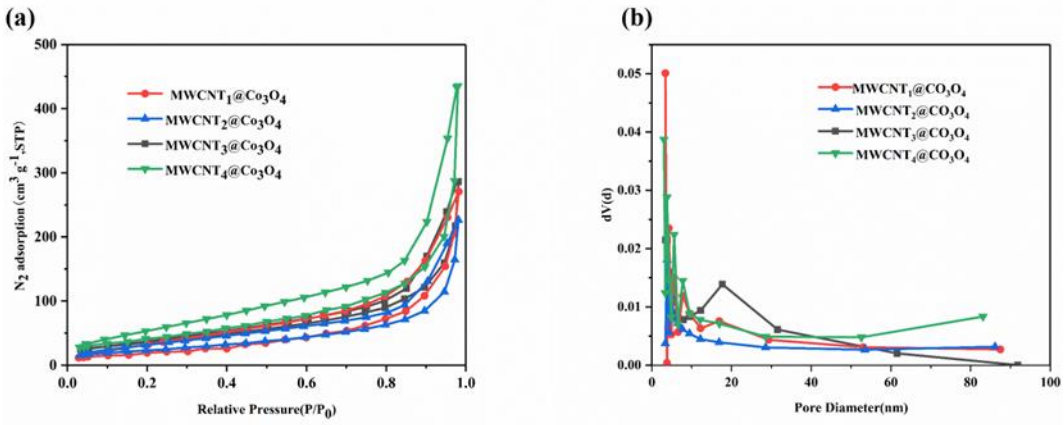

Figure 6. MWCNTx@Co_3O_4 composites (**a**) N_2 adsorption desorption isotherm and (**b**) pore size distribution line.

Figure 7a shows the cyclic voltammetry curves of composites with different carbon nanotube contents at 20 $mV \cdot s^{-1}$. As can be seen, when the scanning speed is 20 $mV \cdot s^{-1}$, the CV curve area of the MWCNT$_3$@Co_3O_4 composite material is the largest, indicating that the addition of appropriate carbon nanotubes can improve the specific capacitance of the electrode. This result can be attributed to the synergistic effect of cobalt tetroxide and carbon nanotubes. MWCNT$_1$@Co_3O_4, MWCNT$_2$@Co_3O_4 and MWCNT$_4$@Co_3O_4 decreased, which may be caused by a too high or too low MWCNT content and the overall electrical conductivity of the material. In addition, obvious redox peaks were observed, which were

mainly due to different cobalt redox states, such as Co^{4+}/Co^{3+} and Co^{3+}/Co^{2+}. The main reaction mechanism is shown in (1) and (2) [43]:

$$Co_3O_4 + OH^- + H_2O \leftrightarrow 3CoOOH + e^- \quad (1)$$

$$CoOOH + OH^- \leftrightarrow CoO_2 + H_2O + e^- \quad (2)$$

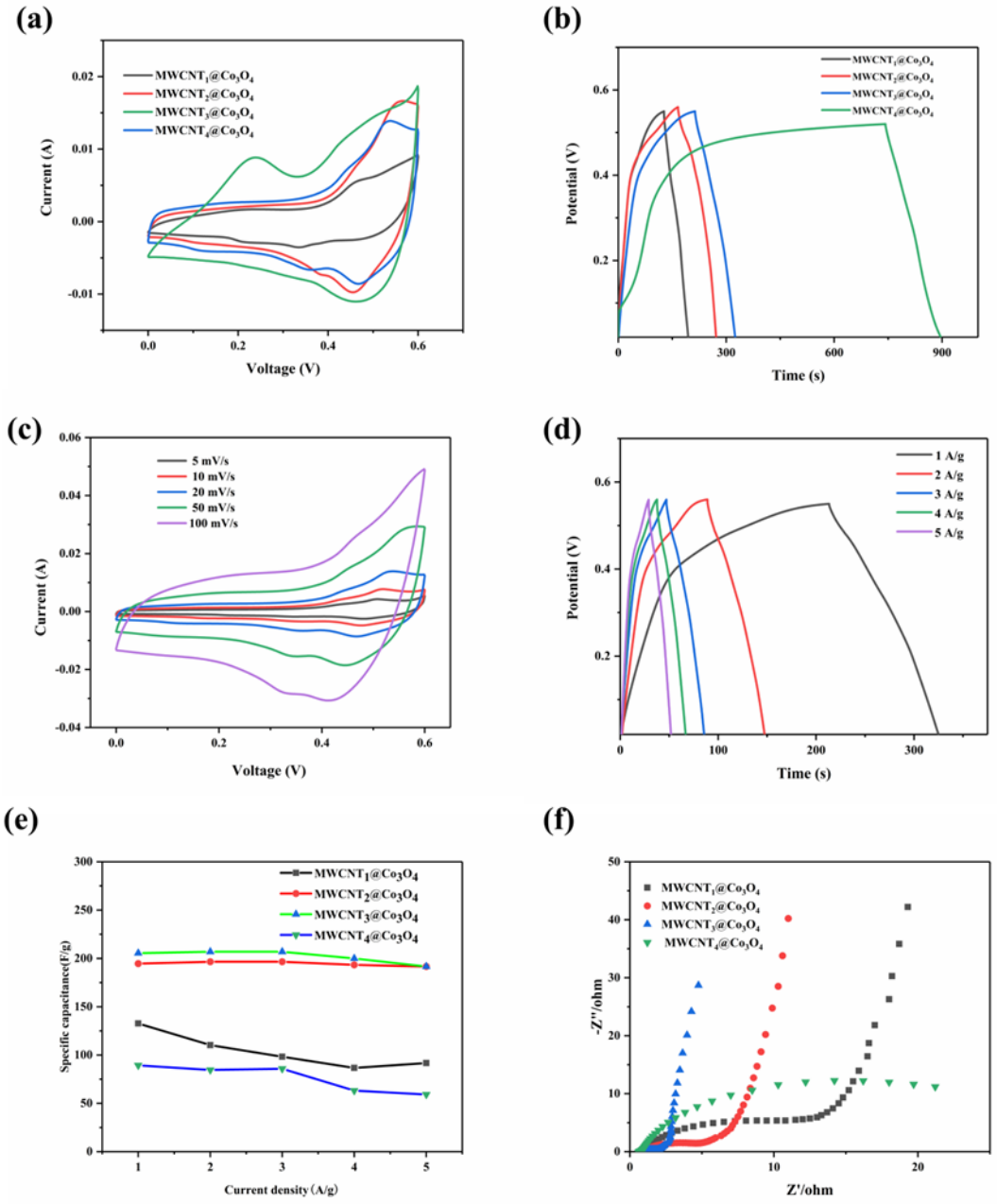

Figure 7. (**a**) CV curve of different mass ratios of $MWCNT_3@Co_3O_4$ composites at 20 $mV \cdot s^{-1}$ sweep velocity; (**b**) GCD curve of the different mass ratios of $MWCNT_3@Co_3O_4$ composites at 1$A \cdot g^{-1}$; (**c**) CV diagram of $MWCNT_3@Co_3O_4$ composite at 20 $mV \cdot s^{-1}$ scanning speed; (**d**) GCD diagram of $MWCNT_3@Co_3O_4$ composites at different current densities; (**e**) magnification performance diagram of the different mass ratios of $MWCNT_3@Co_3O_4$ composites; (**f**) Nyquist diagram of the different mass ratios of $MWCNT_3@Co_3O_4$ composites with an illustration of its local enlarged view.

Figure 7b shows the GCD curve of the MWCNTx@Co_3O_4 composite material, which was tested at a current density of 1 A·g^{-1}. It is observed that the curve is almost triangular in symmetry, and there is no particularly rapid drop in voltage, indicating that the synthesized MWCNT$_1$@Co_3O_4, MWCNT$_2$@Co_3O_4, MWCNT$_3$@Co_3O_4 and MWCNT$_4$@Co_3O_4 materials have particularly good electrochemical reversibility. While the GCD curves of the MWCNT$_4$@Co_3O_4 composite is different from others, its charge time is longer from its discharge time. This is mainly due to the higher resistance, which is consistent with the result of Figure 7f. When applying the same voltage in the MWCNT$_4$@Co_3O_4 composite, the current is unable to charge quickly, which leads to the GCD curve of the sample MWCNT$_4$@Co_3O_4 composite being asymmetrical. The discharge time of MWCNT$_3$@Co_3O_4 is longer than that of MWCNT$_1$@Co_3O_4, MWCNT$_2$@Co_3O_4 and MWCNT$_4$@Co_3O_4. Therefore, among the four materials prepared, the MWCNT$_3$@Co_3O_4 composite has the largest specific capacitance, whereas the MWCNT$_1$@Co_3O_4 composite material has the smallest specific capacitance. It is also comparable to other Co_3O_4-based materials as listed in Table 2.

Table 2. The electrochemical performance of a summary of related Co_3O_4 materials.

Co_3O_4 Materials	**Specific Capacitance (F·g^{-1})**	**Power Density (W·kg^{-1})**	**Energy Density (Wh·kg^{-1})**	**Ref.**
rGO-Co_3O_4	472 F·g^{-1} (2 mV·s^{-1})	39.0	8.3	[44]
Nanostructured Co_3O_4	162 F·g^{-1} (2.75 A·g^{-1})	—-	—-	[45]
Co_3O_4 nanotubes	574 F·g^{-1} (0.1 A·g^{-1})	—-	—-	[46]
Co_3O_4/graphene	362.6 F·g^{-1} (0.72 A·g^{-1})	—-	—-	[47]
$Mn_{0.05}Co_{2.95}O_4$	80.8 F·g^{-1} (1 A·g^{-1})	—-	—-	[48]
Co_3O_4/rGO/NF	311 F·g^{-1} (1 A·g^{-1})	12	40	[49]
MWCNT$_3$@Co_3O_4	206.89 F·g^{-1} (1 A·g^{-1})	800	17.78	This work

Figure 7c shows the cyclic voltammetry curves of MWCNT$_3$@Co_3O_4 at sweep speeds of 5, 10, 20, 50 and 100 mV·s^{-1}. It is observed that the CV curve of the electrode material is similar with an increase in the sweep speed, indicating that the MWCNT$_3$@Co_3O_4 electrode material has good performance. Figure 7d shows the GCD curves of MWCNTx@Co_3O_4 composites at 1, 2, 3, 4 and 5 A·g^{-1} current densities. When the applied current density is 1 A·g^{-1}, the MWCNT$_3$@Co_3O_4 composite has the longest discharge time and its specific capacitance is 206.89 F·g^{-1}, which is higher than MWCNT$_1$@Co_3O_4, MWCNT$_2$@Co_3O_4 and MWCNT$_4$@Co_3O_4 (132.73 F·g^{-1}, 194.64 F·g^{-1}, 89.36 F·g^{-1}, respectively). It is shown that the composite has an excellent electrochemical performance. Figure 7e shows the specific capacitance as a function of current density. As the specific current density increases, the specific capacitance decreases due to the limitation of diffusion on the electrode surface [50]. The MWCNT$_3$@Co_3O_4 electrode shows a specific capacitance of 191.67 F·g^{-1} at 5 A·g^{-1}, and the specific capacity of MWCNT$_3$@Co_3O_4 is 3.2 times higher than that of MWCNT$_4$@Co_3O_4 and 2 times higher than that of MWCNT$_1$@Co_3O_4 at the same current density. By adding an optimal proportion of MWCNT, the capacity of MWCNT@Co_3O_4 is increased, thus promoting the charge-transfer ions on the surface.

Figure 7f shows the electrochemical impedance spectroscopy (EIS) of the MWCNTx@Co_3O_4 composite. It can be observed that the linear slope of the composite is the highest in the low-frequency region MWCNT$_3$@Co_3O_4, which indicates that the ion diffusion resistance of MWCNT$_3$@Co_3O_4 is smaller than that of MWCNT$_1$@Co_3O_4, MWCNT$_2$@Co_3O_4 and MWCNT$_4$@Co_3O_4 electrodes. In the high-frequency region, the MWCNT$_3$@Co_3O_4 electrode has the smallest semicircle diameter, indicating that its charge transfer resistance is smaller than that of MWCNT$_1$@Co_3O_4, MWCNT$_2$@Co_3O_4 and MWCNT$_4$@Co_3O_4, indicating that the charge transfer rate of MWCNT$_3$@Co_3O_4 is faster. It is also further explained that the MWCNT$_3$@Co_3O_4 electrode material has better electrical conductivity.

Figure 8 shows the cycle performance experiment conducted on $MWCNT_3@Co_3O_4$ with a current density of 1 $A \cdot g^{-1}$. As can be seen, the maintenance rate of the specific capacitance of $MWCNT_3@Co_3O_4$ is 78.9% after 1000 cycles of charge and discharge, which indicates that the $MWCNT_3@Co_3O_4$ composite electrode has a good cycle life.

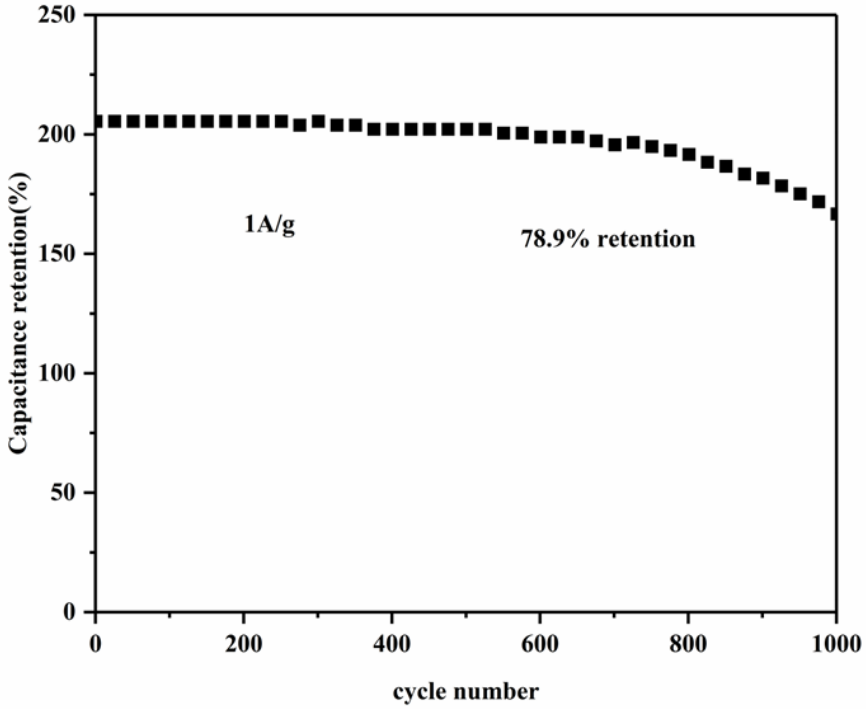

Figure 8. Cycles performance test of $MWCNT_3@Co_3O_4$ at 1 $A \cdot g^{-1}$.

To better explore the practical application of the electrode material, the $MWCNT_3@Co_3O_4$ //AC asymmetric supercapacitor was assembled for the electrochemical test. Figure 9a shows the cyclic voltammetry curves of the $MWCNT_3@Co_3O_4$//AC capacitor at 5, 10, 20, 50 and 100 $mV \cdot s^{-1}$. It can be seen from the figure that the CV curve presents the characteristics of double electric layers and pseudocapacitors, which are the conditions for the capacitor to have a good electrochemical performance. Figure 9b shows the GCD curve under different current densities. The mass specific capacitance of the capacitor under 1, 2, 3, 4 and 5 $A \cdot g^{-1}$ current densities is calculated as 50.0, 46.25, 34.31, 30.0 and 25.0 $F \cdot g^{-1}$, respectively.

Figure 9c shows the relationship between specific current and specific capacitance. It can be seen that the capacitor still has a 57.1% specific capacitance maintenance rate at a current density of 5 $A \cdot g^{-1}$, indicating that the capacitor has an excellent multiplier performance. Figure 9d shows the performance of the device after 1000 cycles. At a 1 $A \cdot g^{-1}$ current density, the initial capacitance remains at 87.2% after 1000 times of charging and discharging, indicating that the capacitor has a good cycle life. This is mainly attributed to the polyhedral structure and high porosity of $MWCNT_3@Co_3O_4$ composites, which reduces the damage of electrode materials during charging and discharging.

Figure 10 shows the relationship between energy density and power density. Under current densities of 1 $A \cdot g^{-1}$, 2 $A \cdot g^{-1}$, 3 $A \cdot g^{-1}$, 4 $A \cdot g^{-1}$ and 5 $A \cdot g^{-1}$, the power densities of the device are 800, 1600, 2400, 3200 and 4000 $W \cdot kg^{-1}$, respectively. The corresponding energy densities are 17.78, 16.44, 12.20, 10.67 and 8.89 $Wh \cdot kg^{-1}$, respectively.

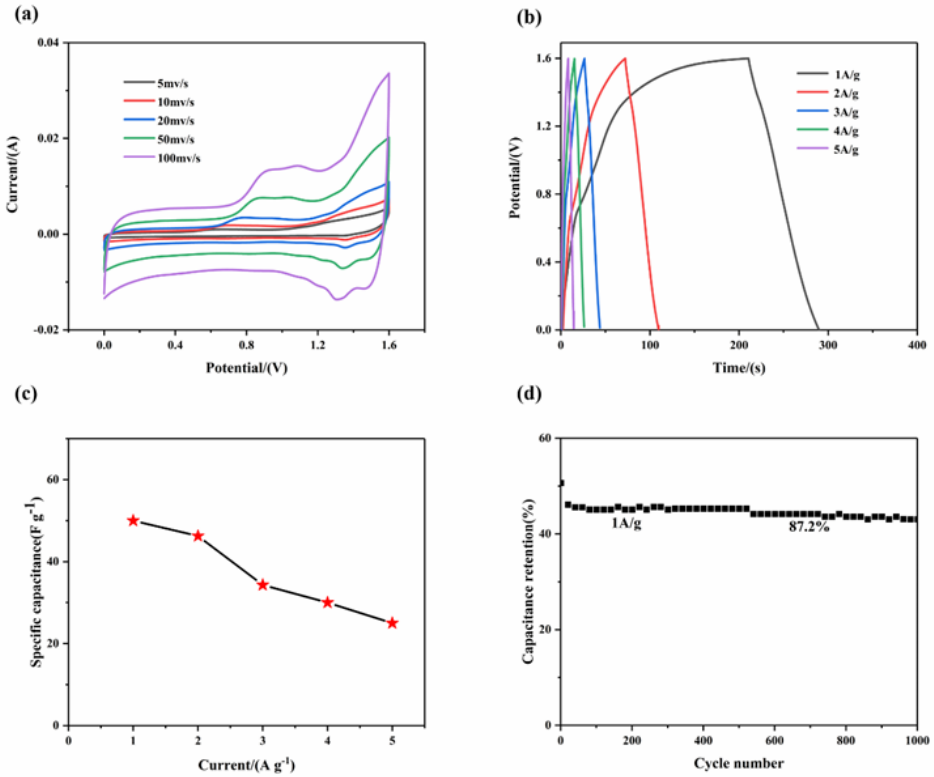

Figure 9. (**a**) Cyclic voltammetry curves at different sweep speeds; (**b**) charge–discharge curves under different current densities; (**c**) relation curve between current density and specific capacitance; (**d**) diagram of 1000 cycles under current density of $MWCNT_3@Co_3O_4//AC$ asymmetric supercapacitor (1 $A \cdot g^{-1}$).

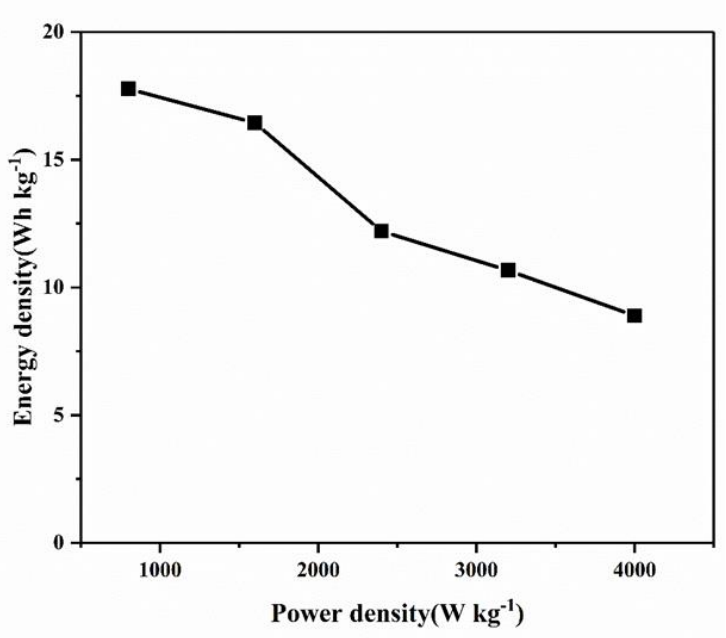

Figure 10. Ragone plots of the symmetrical supercapacitor.

3. Experimental Section

This section may be divided by subheadings. It should provide a concise and precise description of the experimental results and their interpretation, as well as the experimental conclusions that can be drawn.

3.1. Materials

All of the chemical reagents in this experiment were of analytical purity and directly used without any further purification.

3.2. Materials Characterization

XRD analysis was performed by a powder X-ray diffraction system (XRD-6100, Rigaku, Tokyo, Japan) equipped with Cu Kα radiation (λ = 0.15406 nm) to determine crystalline structures of the obtained samples. The XPS measurements were performed by a Thermo ESCALAB 250Xi spectrometer (USA) with monochromated Al Kα radiation (hγ = 1486.6 eV). All XPS spectra were calibrated with respect to the C 1s peak at 284.6 eV. The morphology and microstructure of the samples were characterized by field emission scanning electron microscopy (FE-SEM) (JSM-6480A, JEOL, Tokyo, Japan) and a TEM (JEM-2000FX, Electronics Corporation, Tokyo, Japan). The BET (Brunauer-Emmett-Teller) and pore size distrubtion of the samples were characterized by N_2 adsorption Nitrogen and desorption test (TriStar II3flex, Mike, Scottsdale, AZ, USA).

3.3. Preparation of Materials

Preparation of MWCNTx@ZIF-67 precursor: first, different masses of MWCNT (99.9%, Xianfeng Nanotechnology Co., Ltd., Nanjing, China) were poured into polyethylene pyrrolidone (analytically pure, Shanghai McLean Biochemical Technology Co., Ltd., China) and methanol solution (99.7%, Shanghai Aladdin Co., Ltd., Shanghai, China), ultrasonic was carried out for 30 min, a certain amount of cobalt nitrate (analytically pure, Shanghai Aladdin Biochemical Technology Co., Ltd., Shanghai, China) was added and then magnetic stirring was performed for 10 min. In addition, 2-methylimidazole (≥98.0%, Shanghai McLean Biochemical Technology Co., Ltd., Shanghai, China) was added to the above solution, stirring for 1 h, and then the prepared solution was left to stand at room temperature for 24 h. After centrifugation and washing, the black precipitate was dried at 60 °C for 12 h and the precursor MWCNTx@ZIF-67 was obtained. The weights of MWCNT were 0.0203 g, 0.0415 g, 0.0608 g and 0.1510 g, respectively. Therefore, the resultant MWCNT@ZIF-67 numbers are $MWCNT_1$@ZIF-67, $MWCNT_2$@ZIF-67, $MWCNT_3$@ZIF-67 and $MWCNT_4$@ZIF-67, respectively.

Preparation of MWCNTx@Co_3O_4 composite: the synthesized precursors ($MWCNT_1$@ZIF-67, $MWCNT_2$@ZIF-67 and $MWCNT_3$@ZIF-67, $MWCNT_4$@ZIF-67) were annealed in air at 350 °C for 2 h at a heating rate of 4 °C·min^{-1}. The obtained samples were labeled $MWCNT_1$@Co_3O_4, $MWCNT_2$@Co_3O_4, $MWCNT_3$@Co_3O_4 and $MWCNT_4$@Co_3O_4.

3.4. Fabrication of Supercapacitor Electrode

(1) Preparation of Single Electrode

All single electrodes in this paper were prepared in the following way: firstly, certain amounts of active substance and acetylene black (Superconducting K90, Ron reagent, Harbin, China) were weighed, dissolved in 5 mL of absolute ethanol and ultrasonicated for 30 min. Then, a certain amount of PTFE (60.0 wt%, Shanghai Aladdin Biochemical Technology Co., Ltd., Shanghai, China) lotion (the mass ratio of active substance, acetylene black and PTFE lotion (5wt%) was 8:1:1) was dropped in proportion, ultrasonicated for 10 min and then dried in a constant temperature blast-drying oven at 60 °C for 12 h. Finally, the obtained black sample was scraped onto one side of foam nickel of 1 × 1 cm, pressed with a tablet press and compacted evenly. By weighing the total mass of foam nickel before and after scraping, the total mass of active substance can be calculated.

(2) Assembly of Asymmetric Supercapacitors

In order to evaluate the practical application of the prepared electrode material, the electrode material and AC prepared in this article were used to prepare a single electrode in the same manner as in (1). Subsequently, when assembling the supercapacitor, they were assembled on the positive electrode and the negative electrode of the supercapacitor, respectively. At the same time, the positive and negative electrodes were separated by

a membrane, and an asymmetric supercapacitor was assembled. The electrolyte was prepared as a 3.0 M KOH (≥85.0%, Shanghai Aladdin Biochemical Technology Co., Ltd., Shanghai, China) solution.

3.5. Electrochemical Characterization

Electrochemical workstation (CHI 760E) was used to observe the electrochemical performance of the MWCNTx@Co_3O_4 composite electrode in a three-electrode installation. In this test, platinum was used as a counter electrode, Ag/AgCl as a reference electrode, MWCNTx@Co_3O_4 composites as a working electrode and a solution of 3 M KOH as electrolyte. Cyclic voltammetry (CV) was performed between 0 V and 0.6 V at various scan rates (from 5 to 100 $mV \cdot s^{-1}$). Galvanostatic discharge texts were measured in a voltage window from 0 V to 0.55 V at various current densities. EIS measurements were carried out with a 5 mV sinusoidal voltage in a frequency from 100 kHz to 0.01 Hz.

4. Conclusions

In summary, a diamond-dodecahedron-structured $MWCNT_x$@Co_3O_4 composite was successfully fabricated using a smart approach. With an increase in the MWCNT content, the electrochemical properties of the $MWCNT_X$@Co_3O_4 composite first increased and then decreased. Benefiting from the unique structure, high specific surface area and reasonable pore size distribution, the as-obtained $MWCNT_3$@Co_3O_4 composite exhibits satisfactory capacitive behavior: 206.89 $F \cdot g^{-1}$ at a current density of 1 $A \cdot g^{-1}$; an excellent cycling stability of 87.2% capacitance retention over 1000 continuous cycles. An asymmetric supercapacitor cell was fabricated through MWCNTx@Co_3O_4 and AC as a positive and negative electrode, respectively. The cell can deliver a high energy density of 17.78 $Wh \cdot kg^{-1}$ at a power density of 800 $W \cdot kg^{-1}$. Our results suggest that the MWCNTx@Co_3O_4 composite can be used in actual high-power devices. The preparation strategy offers a facile and variable route to rationally design and prepare cobalt oxide electrode materials for a variety of applications in energy storage and conversion, catalysis and environmental treatment.

Author Contributions: Conceptualization, methodology, writing—original draft preparation, C.Y.; software, validation, X.S.; investigation, H.L.; software, validation, investigation, writing—review and editing, L.T.; data curation, W.L.; visualization, X.L. All authors have read and agreed to the published version of the manuscript.

Funding: This research was funded by the Outstanding Youth Project of Natural Science Foundation in Heilongjiang Province (YQ2022E040), the Natural Science Foundation of Shandong Province of China (ZR2022ME166), the Postdoctoral Scientific Research Developmental Fund of Heilongjiang Province (LBH-Q20023), the University Nursing Program for Young Scholars with Creative Talents in Heilongjiang Province (UNPYSCT-2020197).

Institutional Review Board Statement: Not applicable.

Informed Consent Statement: Not applicable.

Data Availability Statement: Not applicable.

Acknowledgments: This work was financially supported by the Outstanding Youth Project of Natural Science Foundation in Heilongjiang Province (YQ2022E040), the Natural Science Foundation of Shandong Province of China (ZR2022ME166), the Postdoctoral Scientific Research Developmental Fund of Heilongjiang Province (LBH-Q20023), the University Nursing Program for Young Scholars with Creative Talents in Heilongjiang Province (UNPYSCT-2020197).

Conflicts of Interest: The authors declare that they have no known competing financial interests or personal relationships that could have appeared to influence the work reported in this paper.

Sample Availability: Samples of the compounds MWCNTx@Co_3O_4 are available from the authors.

References

1. Liu, C.; Li, F.; Ma, L.P.; Cheng, H.M. Advanced Materials for Energy Storage. *Adv. Mater.* **2010**, *22*, 28–62. [CrossRef] [PubMed]
2. Brousse, T.; Taberna, P.L.; Crosnier, O.; Dugas, R.; Guillemet, P.; Scudeller, Y.; Zhou, Y.; Favier, F.; Belanger, D.; Simon, P.J. Long-term cycling behavior of asymmetric activated carbon/MnO_2 aqueous electrochemical supercapacitor. *J. Power Sources* **2007**, *173*, 633. [CrossRef]
3. Yuan, C.Z.; Zhang, X.G.; Su, L.H.; Gao, B.; Shen, L.F. Facile synthesis and self-assembly of hierarchical porous NiO nano/micro spherical superstructures for high performance supercapacitors. *J. Mater. Chem.* **2009**, *19*, 5772. [CrossRef]
4. Najib, S.; Erdem, E. Current progress achieved in novel materials for supercapacitor electrodes: Mini review. *Nanoscale Adv.* **2019**, *1*, 2817–2827. [CrossRef] [PubMed]
5. Sarangapani, S.; Tilak, B.V.; Chen, C.P. Materials for electrochemical capacitors: Theoretical and experimental constraints. *J. Electrochem. Soc.* **1996**, *143*, 3761. [CrossRef]
6. Gherghel, L.; Kubel, C.; Lieser, G.; Rader, H.J.; Mullen, K.J. Pyrolysis in the mesophase: A chemist's approach toward preparing carbon nano-and microparticles. *Am. Chem. Soc.* **2002**, *124*, 13130–13138. [CrossRef] [PubMed]
7. Titirici, M.M.; Antonietti, M. Chemistry and materials options of sustainable carbon materials made by hydrothermal carbonization. *Chem. Soc. Rev.* **2010**, *39*, 103–116. [CrossRef] [PubMed]
8. Elmouwahidi, A.; Zapata-Benabithe, Z.; Carrasco-Marin, F.; Moreno-Castilla, C. Activated carbons from KOH-activation of argan (Argania spinosa) seed shells as supercapacitor electrodes. *Bioresour. Technol.* **2012**, *111*, 185–190. [CrossRef]
9. Liang, Q.; Ye, L.; Huang, Z.H.; Xu, Q.; Bai, Y.; Kang, F.; Yang, Q.H. A honeycomb-like porous carbon derived from pomelo peel for use in high-performance supercapacitors. *Nanoscale* **2014**, *6*, 13831–13837. [CrossRef]
10. Yang, Z.-C.; Tang, C.-H.; Gong, H.; Li, X.; Wang, J.J. Hollow spheres of nanocarbon and their manganese dioxide hybrids derived from soft template for supercapacitor application. *Power Sources* **2013**, *240*, 713–720. [CrossRef]
11. Luo, C.; Wei, R.; Guo, D.; Zhang, S.; Yan, S. Adsorption behavior of MnO_2 functionalized multi-walled carbon nanotubes for the removal of cadmium from aqueous solutions. *Chem. Eng. J.* **2013**, *225*, 406–415. [CrossRef]
12. Xie, X.; Gao, L. Characterization of a manganese dioxide/carbon nanotube composite fabricated using an in situ coating method. *Carbon* **2007**, *45*, 2365–2373. [CrossRef]
13. Yang, B.; Gong, Q.; Zhao, L.; Sun, H.; Ren, N.; Qin, J.; Xu, J.; Yang, H. Preconcentration and determination of lead and cadmium in water samples with a MnO_2 coated carbon nanotubes by using ETAAS. *Desalination.* **2011**, *278*, 65–69. [CrossRef]
14. Li, B.; Bai, C.; Zhang, S.; Zhao, X.; Li, Y.; Wang, L.; Ding, K.; Shu, X.; Li, S.; Ma, L.J. An adaptive supramolecular organic framework for highly efficient separation of uranium via an in situ induced fit mechanism. *J. Mater. Chem. A* **2015**, *3*, 23788–23798. [CrossRef]
15. Huang, L.; Li, C.; Yuan, W.; Shi, G. Strong composite films with layered structures prepared by casting silk fibroin–graphene oxide hydrogels. *Nanoscale* **2013**, *5*, 3780–3786. [CrossRef]
16. Gupta, T.K.; Singh, B.P.; Singh, V.N.; Teotia, S.; Singh, A.P.; Elizabeth, I.; Dhakate, S.R.; Dhawan, S.; Mathur, R.J. MnO_2 decorated graphene nanoribbons with superior permittivity and excellent microwave shielding properties. *J. Mater. Chem. A* **2014**, *2*, 4256–4263. [CrossRef]
17. Wei, L.S.; Deng, W.J.; Li, S.S.; Wu, Z.G.; Cai, J.H.; Luo, J.W. Sandwich-like chitosan porous carbon Spheres/MXene composite with high specific capacitance and rate performance for supercapacitors. *J. Bioresour. Bioprod.* **2022**, *7*, 63–72. [CrossRef]
18. Hsu, S.C.; Chiang, H.H.; Huang, T.Y.; Chao, S.H.; Wu, R.T.; Huang, J.-H.; Chang-jian, C.W.; Weng, H.C.; Chen, H.C. Morphology evolution and electrochemical behavior of $Ni_xMn_{1-x}(OH)_2$ mixed hydroxides as high-performance electrode for supercapacitor. *J. Electrochim. Acta* **2022**, *403*, 139692. [CrossRef]
19. Yang, G.W.; Xu, C.L.; Li, H.L. Electrodeposited nickel hydroxide on nickel foam with ultrahigh capacitance. *Chem.Commun.* **2008**, 6537–6539. [CrossRef] [PubMed]
20. Hsiao, Y.-S.; Chang-Jian, C.-W.; Huang, T.-Y.; Chen, Y.-L.; Huang, J.-H.; Wu, N.-J.; Hsu, S.-C.; Cheng, C.-P. High-performance supercapacitor based on a ternary nanocomposites of NiO, polyaniline, and Ni/NiO-decorated MWCNTs. *J. Taiwan Inst. Chem. Eng.* **2022**, *134*, 104318. [CrossRef]
21. Zhang, H.; Cao, G.; Wang, Z.; Yang, Y.; Shi, Z.; Gu, Z. Growth of manganese oxide nanoflowers on vertically-aligned carbon nanotube arrays for high-rate electrochemical capacitive energy storage. *Nano Lett.* **2008**, *8*, 2664. [CrossRef]
22. Zhu, T.; Chen, J.S.; Lou, X.W. Shape-controlled synthesis of porous Co_3O_4 nanostructures for application in supercapacitors. *J. Mater. Chem.* **2010**, *20*, 7015. [CrossRef]
23. Zhang, G.; Chen, Y.; Qu, B.; Hu, L.; Mei, L.; Lei, D.; Li, Q.; Chen, L.; Li, Q.; Wang, T. Synthesis of mesoporous NiO nanospheres as anode materials for lithium ion batteries. *Electrochim. Acta* **2012**, *80*, 140–147. [CrossRef]
24. Bae, J.; Song, M.K.; Park, Y.J.; Kim, J.M.; Liu, M.; Wang, Z.L. Fiber supercapacitors made of nanowire-fiber hybrid structures for wearable/flexible energy storage. *Angew. Chem. Int. Ed.* **2011**, *50*, 1683. [CrossRef]
25. Yuan, L.; Lu, X.H.; Xiao, X.; Zhai, T.; Dai, J.; Zhang, F.; Hu, B.; Wang, X.; Gong, L.; Chen, J.; et al. Flexible Solid-State Supercapacitors Based on Carbon Nanoparticles/MnO_2 Nanorods Hybrid Structure. *ACS Nano* **2012**, *6*, 656. [CrossRef]
26. Yang, P.H.; Xiao, X.; Li, Y.Z.; Ding, Y.; Qiang, P.F.; Tan, X.H.; Mai, W.J.; Lin, Z.Y.; Wu, W.Z.; Li, T.Q.; et al. Hydrogenated ZnO core–shell nanocables for flexible supercapacitors and self-powered systems. *ACS Nano* **2013**, *7*, 2617. [CrossRef]
27. Xiao, Z.Y.; Fan, L.L.; Xu, B.; Zhang, S.Q.; Kang, W.P.; Kanga, Z.X.; Lin, H.; Liu, X.P.; Zhang, S.Y.; Sun, D.F. Green Fabrication of Ultrathin Co_3O_4 Nanosheets from Metal–Organic Framework for Robust High-Rate Supercapacitors. *ACS Appl. Mater. Interfaces* **2017**, *9*, 41827–41836. [CrossRef]

28. Huang, X.H.; Tu, J.P.; Xia, X.H.; Wang, X.L.; Xiang, J.Y. Porous NiO/poly (3, 4-ethylenedioxythiophene) films as anode materials for lithium ion batteries. *J. Power Sources* **2010**, *195*, 1207–1210. [CrossRef]
29. Li, W.; Xu, L.; Chen, J. Co_3O_4 Nanomaterials in Lithium-Ion Batteries and Gas Sensors. *Adv. Funct. Mater.* **2005**, *15*, 851–857. [CrossRef]
30. Xu, W.; Chen, J.H.; Yu, M.H.; Zeng, Y.X.; Long, Y.B.; Lu, X.H.; Tong, Y.X. Sulphur-doped Co_3O_4 nanowires as an advanced negative electrode for high-energy asymmetric supercapacitors. *J. Mater. Chem. A* **2016**, *4*, 10779–10785. [CrossRef]
31. Simon, P.; Gogotsi, Y. Capacitive energy storage in nanostructured carbon-electrolyte systems. *Acc. Chem. Res.* **2013**, *46*, 1094–1103. [CrossRef]
32. Zhang, Y.; Feng, H.; Wu, X.; Wang, L.; Zhang, A.; Xia, T.; Dong, H.; Li, X.; Zhang, L. Progress of electrochemical capacitor electrode materials: A review. *Int. J. Hydrog. Energy* **2009**, *34*, 4889–4899. [CrossRef]
33. Wang, G.; Zhang, L.; Zhang, J. A review of electrode materials for electrochemical supercapacitors. *Chem. Soc. Rev.* **2012**, *41*, 797–828. [CrossRef]
34. Su, D.S.; Schlögl, R. Nanostructured carbon and carbon nanocomposites for electrochemical energy storage applications. *Chem. Sus. Chem.* **2010**, *3*, 136–168. [CrossRef]
35. Zheng, S.; Zhang, J.W.; Deng, H.B.; Du, Y.M.; Shi, X.W. Chitin derived nitrogen-doped porous carbons with ultrahigh specific surface area and tailored hierarchical porosity for high performance supercapacitors. *J. Bioresour. Bioprod.* **2021**, *6*, 142–151. [CrossRef]
36. Yan, B.; Feng, L.; Zheng, J.J.; Zhang, Q.; Jiang, S.H.; Zhang, C.M.; Ding, Y.C.; Han, J.Q.; Chen, W.; He, S.J. High performance supercapacitors based on wood-derived thick carbon electrodes synthesized via green activation process. *Inorg. Chem. Front.* **2022**, *9*, 6108–6123. [CrossRef]
37. Zhang, C.; Wang, Q.; Zhang, W.; Li, X.; Zhu, Z.; Zhang, C.; Xie, A.; Luo, S. Preparation and application of Co_3O_4-Ni-MOF/MWCNTs hybrid for supercapacitor. *Ionics* **2021**, *27*, 3543–3551. [CrossRef]
38. Wang, X.; Li, M.; Chang, Z.; Yang, Y.; Wu, Y.; Liu, X. Co_3O_4@MWCNT Nanocable as Cathode with Superior Electrochemical Performance for Supercapacitors. *ACS Appl. Mater. Interfaces* **2015**, *7*, 2280–2285. [CrossRef]
39. Ma, J.X.; Li, J.; Guo, R.; Xu, H.; Shi, F.; Dang, L.Q.; Liu, Z.H.; Sun, J.; Lei, Z.H. Direct growth of flake-like metal-organic framework on textile carbon cloth as high-performance supercapacitor electrode. *J. Power Sources* **2019**, *428*, 124–130. [CrossRef]
40. Kumar, Y.A.; Das, H.T.; Guddeti, P.R.; Nallapureddy, R.R.; Pallavolu, M.R.; Alzahmi, S.; Obaidat, I.M. Self-Supported Co_3O_4@Mo-Co_3O_4 Needle-like Nanosheet Heterostructured Architectures of Battery-Type Electrodes for High-Performance Asymmetric Supercapacitors. *Nanomaterials* **2022**, *12*, 2330. [CrossRef]
41. Ramesh, S.; Karuppasamy, K.; Sivasamy, A.; Kim, H.S.; Yadav, H.M.; Kim, H.S. Core shell nanostructured of Co_3O_4@RuO_2 assembled on nitrogen-doped graphene sheets electrode for an efficient supercapacitor application. *J. Alloy. Compd.* **2021**, *877*, 160297. [CrossRef]
42. Zhu, S.Q.; Shu, J.C.; Cao, M.S. Novel MOF-derived 3D hierarchical needlelike array architecture with excellent EMI shielding, thermal insulation and supercapacitor performance. *Nanoscale* **2022**, *14*, 7322–7331. [CrossRef]
43. Sivakumar, P.; Jana, M.; Kota, M.; Jung, M.; Gedanken, A.; Park, H.S. Controllable synthesis of nanohorn-like architectured cobalt oxide for hybrid supercapacitor application. *J. Power Sources* **2018**, *402*, 147–156. [CrossRef]
44. Xiang, C.C.; Li, M.; Zhi, M.J.; Manivannan, A.; Wu, N.Q. A reduced graphene oxide/Co_3O_4 composite for supercapacitor electrode. *J. Power Sources* **2013**, *3*, 65–70. [CrossRef]
45. Tummala, R.; Guduru, R.K.; Mohanty, P.S. Nanostructured Co_3O_4 electrodes for supercapacitor applications from plasma spray technique. *J. Power Sources* **2012**, *209*, 44–51. [CrossRef]
46. Xu, J.; Gao, L.; Cao, J.Y.; Wang, W.C.; Chen, Z.D. Preparation and electrochemical capacitance of cobalt oxide (Co_3O_4) nanotubes as supercapacitor material. *Electrochim. Acta* **2010**, *56*, 732–736. [CrossRef]
47. Zhou, Y.L.; Hu, Z.B.; Zhao, C.H.; Liu, K.Y.; Lin, D.G. Synthesis and Electrochemical Performances of Co_3O_4/graphene as Supercapacitor Material. *Int. J. Electrochem. Sci.* **2016**, *11*, 6078–6084. [CrossRef]
48. Aslam, S.; Ramay, S.M.; Mahmood, A.; Mustafa, M.G.; Zawar, S.; Atiq, S. Electrochemical performance of transition metal doped Co3O4 as electrode material for supercapacitor applications. *J. Sol-Gel. Sci. Technol.* **2023**, *105*, 360–369. [CrossRef]
49. Wang, X.Y.; Lu, S.X.; Xu, W.G. Synthesis of Needle-like Nanostructure Composite Electrode of Co_3O_4/rGO/NF for High-Performance Symmetric Supercapacitor. *Crystals* **2022**, *12*, 664. [CrossRef]
50. Sudhakaran, M.S.P.; Gnanasekaran, G.; Pazhamalai, P.; Sahoo, S.; Hossain, M.M.; Bhattarai, R.M.; Kim, S.J.; Mok, Y.S. Hierarchically Porous Nanostructured Nickel Phosphide with Carbon Particles Embedded by Dielectric Barrier Discharge Plasma Deposition as a Binder-Free Electrode for Hybrid Supercapacitors. *ACS Sustain. Chem. Eng.* **2019**, *7*, 14805–14814.